Numerical Study of the Optimization of Separation Control

Angelo Carnarius[*], Bert Günther[*] and Frank Thiele[†]

Technical University of Berlin, Berlin, 10623, Germany

Daniel Wachsmuth[‡] and Fredi Tröltzsch[§]

Technical University of Berlin, Berlin, 10623, Germany

Juan Carlos de los Reyes[¶]

Escuela Politécnica Nacional Quito, Quito, Ecuador

The concept of active flow control is applied to the steady flow around a NACA4412 and to the unsteady flow around a generic high-lift configuration in order to delay separation. To the former steady suction upstream of the detachment position is applied. In a series of computations the suction angle β is varied and the main flow features are analyzed. A gradient descent method and an adjoint-based method are successfully used to optimize β. For the unsteady case periodic blowing and suction is employed to control the separation. Various calculations are conducted to obtain the dependency of the lift on the amplitude and frequency of the perturbation and the amplitude is optimized with the gradient descent method.

Nomenclature

c, c_k	chord length of the main airfoil, chord length of the flap
c_l, c_l^*	lift coefficient, normalized lift coefficient
c_p	pressure coefficient
C_μ	momentum coefficient
f	frequency, control
J	objective function
q	adjoint pressure
Re	Reynolds number
St	Strouhal number
u_{abs}, u_p, u_∞	velocity magnitude, amplitude of excitation, free stream velocity
u_i	velocity vector
y^+	non-dimensional wall distance
w_i	adjoint velocity vector
α	angle of attack
β, β^*	suction angle, normalized suction angle
δ, δ_f	slot angle, flap deflection angle
γ	weighting factor
μ, μ_{eff}	viscosity, effective viscosity
ϱ	density

[*]Research Associate, Institute of Fluid Mechanics and Engineering Acoustics, Müller–Breslau–Straße 8, AIAA Student Member.

[†]Professor, Institute of Fluid Mechanics and Engineering Acoustics, Müller–Breslau–Straße 8, AIAA Member.

[‡]Research Associate, Institute of Mathematics, Straße des 17. Juni 136.

[§]Professor, Institute of Mathematics, Straße des 17. Juni 136.

[¶]Professor, Departamento de Matemática, Ladrón de Guevara E11-253.

American Institute of Aeronautics and Astronautics

I. Introduction

During take-off and landing, the wings of airplanes have to generate an enormous amount of lift at low flight velocity. In modern commercial aircraft, this is realized by complex multi-element high-lift devices. As these cause additional weight, increased constructive effort, etc., there exists a significant economical interest in replacing the multi-element devices by single flaps. However, such flaps are only applicable if flow separation at high flap angles can be controlled.

One possibility for active separation control is suction and/or blowing. In previous studies it has been demonstrated that this mechanism is very effective in delaying separation.[4–6] Most applications incorporate excitation at the leading edge in order to affect the boundary layer upstream of the point of separation,[8] with periodic suction and blowing often proving superior to simple steady blowing or suction. The choice of the optimal excitation parameters (e.g. frequency, amplitude, position, direction of blowing/suction) is case-dependent. The more excitation parameters that are considered in the design of the control mechanism, the more difficult it is to determine the optimal parameter combination. Whereas a single parameter might be varied manually in a series of simulations in order to find its optimal value, an optimal set of several parameters has to be found by different means.

In the present paper, two gradient-based optimization strategies are studied in order to reduce the effort in finding the optimal set of control parameters. The first is a gradient descent method, which is easily implemented but lacks numerical efficiency with an increasing amount of excitation parameters. The second is an adjoint method, requiring complex implementation but enabling efficient computation even for a larger number of parameters.

II. Flow Configurations

Two different aerodynamic flow configurations were chosen to study the optimization strategies. The first one is the steady flow around a single NACA4412 airfoil. This configuration was used for validation of the implementation of the two optimization methods and to gain experience with their numerical behavior. The second one is the unsteady flow around a generic high-lift configuration, which is a more complex test case with practical relevance. So far, only the gradient descent method has been tested in detail with the second configuration.

A. Steady Case

Results for two different angles of attack (AoA), namely $\alpha = 9°$ and $\alpha = 14°$, are presented. The Reynolds number was $Re = 10^6$ based on the chord length c and the free stream velocity u_∞. In fig. 1 the computational domain and a section of the mesh of this two-dimensional configuration is shown. The grid consists of approximately 42000 control volumes and is refined towards the wall yielding a non-dimensional wall distance of $y^+ \leq 1$ for the first inner grid point. The domain is divided into four blocks for parallel computing on 4 CPUs. At the inlet boundaries and the perturbation slot the velocities were prescribed. A no-slip boundary condition was used for the remaining airfoil surface and a standard Neumann boundary condition was applied at the outflow. For this test case, steady suction with a constant amplitude of $u_p/u_\infty = 1$ was used to control the flow separation and increase the lift. The slot width and location was $H/c = 0.0128, x/c = 0.835$ for $\alpha = 9°$ and $H/c = 0.0192, x/c = 0.382$ for $\alpha = 9°$ and it was resolved by two control volumes. The perturbation parameter to be optimized was the angle of the perturbation velocity vector relative to the wing surface of a closed slot, denoted suction angle β in the following.

B. Unsteady Case

A sketch of the 2D generic high-lift configuration is shown in fig. 2, which has been previously investigated in the context of flow control.[1,4,5,8] It consists of a NACA4412 main airfoil at $\alpha = 3°$ AoA and a NACA4415 flap with a deflection angle of $\delta_f = 37°$. The main airfoil is mounted at 52% of the tunnel height and the flap is located underneath the trailing edge forming a gap of $FG = 0.078c$ with an overlap of $FO = 0.027c$. The flow was computed at $Re = 160000$, based on the main element's chord and the free stream velocity. At this Reynolds number, the high deflection angle of the flap causes separation of the flow near the leading edge at $\frac{x}{c_k} \approx 2.8\%$ and leads to a significant loss of lift.

American Institute of Aeronautics and Astronautics

To delay the flow separation and increase the lift, periodic suction and blowing on the flap with zero net-mass-flux and a fixed non-dimensional frequency of $St = \frac{f c_k}{u_\infty} = 0.55$ was used. The slot was located near the leading edge at $x/c_k = 0.031$ and had a width of $H/c_k = 0.004$. The parameter to be optimized for this unsteady test case was the excitation amplitude. It was varied from $u_p = 0\,\mathrm{m/s}$ to $u_p = 12.619\,\mathrm{m/s}$, which matches a non-dimensional momentum coefficient of $C_\mu = \frac{H}{c}\frac{u^2}{u_\infty^2} = 0$ to $C_\mu = 130 \cdot 10^{-5}$. The direction of the excitation was perpendicular to the flap surface.

As can be seen in fig. 2, a strong blockage of the wind tunnel exists due to the short distance between the airfoil and the tunnel walls. Hence, these walls were included in the computational domain. A block-structured mesh with approximately 36500 control volumes was used for the simulations, see fig. 3. At the wing surface, no-slip conditions were applied and all boundaries were resolved ($y^+ < 1$ for first grid point). The tunnel walls were modeled as Euler-walls in order to account for the blockage and at the outlet a Neumann condition was chosen.

III. Methods

A. Numerical Method

For the numerical simulation of the test cases described above, the fully implicit, pressure-based, general Finite-Volume code ELAN[13] was used to solve the (unsteady) Reynolds-averaged Navier-Stokes equations. The flow solver is formulated in curvilinear coordinates and is of second order accuracy in time and space. Convective fluxes are approximated by a TVD-scheme. The pressure is calculated in a SIMPLE-based algorithm with co-located storage arrangement using a generalized Rhie & Chow-Interpolation. The flow solver is parallelized by domain decomposition and uses MPI for the communication between the nodes of the parallel computer. To account for the turbulent fluid motion the Wilcox k-ω turbulence model[12] was used.

The flow control was realized by prescribing the velocities at the perturbation slot according to eq. 1, which has been successfully applied to flow control in previous studies.[6, 11]

$$\underline{u} = u_p \cdot \underline{r} \cdot F(t), \quad \underline{r} = \begin{pmatrix} \cos\left(\beta - \delta\right) \\ \sin\left(\beta - \delta\right) \end{pmatrix}, \quad F(t) = \begin{cases} \sin\left[2\pi f\left(t - t_0\right)\right] & \text{unsteady case} \\ 1 & \text{steady case} \end{cases} \tag{1}$$

In the above equation, u_p is the perturbation amplitude, f is the perturbation frequency, t_0 is a reference time, β is the suction angle and δ is the angle of the perturbation slot.

B. Optimization

Both of the gradient-based methods require several simulations of the flow with varying perturbation quantities. In every optimization cycle, a gradient of the objective function J is calculated. This gradient is weighted by a factor γ to determine the improved quantity ϕ_{new}:

$$\phi_{new} = \phi_{old} + \gamma \nabla J \tag{2}$$

The factor γ is readapted during the optimization in order to guarantee that the new perturbation quantity obeys certain constraints. For the cases studied here, the objective function is the lift coefficient and the constraints are:

$$c_l(\phi_{new}) \quad > \quad c_l(\phi_{old}) \tag{3}$$
$$\phi_{min} \leq \quad \phi_{new} \quad \leq \phi_{max} \tag{4}$$

As stop criterion the normalized change of the lift coefficient between two optimization cycles had to be sufficiently small:

$$\left| \frac{c_l(\phi_{new}) - c_l(\phi_{old})}{c_l(\phi_{old})} \right| \leq \epsilon \tag{5}$$

1. Gradient Descent Method

With the gradient descent method, the gradient ∇J is directly calculated from the lift coefficient of two subsequent computations:

$$\nabla J = \frac{c_l(\phi_{old} + \Delta\phi) - c_l(\phi_{old})}{\Delta\phi} \tag{6}$$

The choice of the weighting factor γ is essential for an application of the method to flow configurations with practical relevance. If the starting value of γ is too low, the number of optimization cycles needed to obtain convergence in a reasonable time is far too high. In a variety of test calculations it has turned out to be a good practice to choose a rather high value for γ and to limit the maximum change of ϕ:

$$\phi_{new} = \phi_{old} + \max\left(d\phi_{max}, \gamma\nabla J\right) \tag{7}$$

For the results shown below, the maximum change has been fixed to $d\phi_{max} = 2.5 \cdot \Delta\phi$.

2. Adjoint Method

So far, adjoint-based optimization is usually used for simple flow configurations at low Re-numbers.[3,7,9,10] Although an application to unsteady, turbulent problems is possible the computational expense is very high.[2] In the presented studies, an adjoint-based optimization has been used for the separation control of a steady turbulent flow at a high Re-number. This requires a complete set of adjoint transport equations and boundary conditions to be implemented and solved for the domain Ω.

$$\frac{\partial w_i}{\partial x_i} = S \qquad \text{in } \Omega \tag{8}$$

$$-\varrho u_j \frac{\partial w_i}{\partial x_j} + \frac{\partial q}{\partial x_i} - \frac{\partial}{\partial x_j}\left[\mu_{eff}\left(\frac{\partial w_i}{\partial x_j} + \frac{\partial w_j}{\partial x_i}\right)\right] + \varrho w_j \frac{\partial u_j}{\partial x_i} = S_i \qquad \text{in } \Omega \tag{9}$$

In the above equations, u_i is the velocity of the RANS-solution, w_i is the adjoint velocity, q is the adjoint pressure and S, S_i are additional source terms. The exact formulation of the source terms and conditions on the boundaries Γ depends on the objective function and is therefore case-dependent. The same holds for the gradient which must be calculated in order to evaluate equation 2. For the test cases studied here, the objective is to maximize the lift coefficient c_l. In combination with the boundary conditions described in section II, the following set of adjoint equations has to be solved:

$$\frac{\partial w_i}{\partial x_i} = 0 \qquad \text{in } \Omega \tag{10}$$

$$-\varrho u_j \frac{\partial w_i}{\partial x_j} + \frac{\partial q}{\partial x_i} - \frac{\partial}{\partial x_j}\left[\mu_{eff}\left(\frac{\partial w_i}{\partial x_j} + \frac{\partial w_j}{\partial x_i}\right)\right] + \varrho w_j \frac{\partial u_j}{\partial x_i} = 0 \qquad \text{in } \Omega \tag{11}$$

$$w_i = 0 \qquad \text{on } \Gamma_{walls,inlet} \tag{12}$$

$$w_i = e_i \qquad \text{on } \Gamma_{airfoil} \tag{13}$$

$$\mu\left(\frac{\partial w_i}{\partial x_j} + \frac{\partial w_j}{\partial x_i}\right)n_j - qn_i + \varrho u_j n_j w_i = 0 \qquad \text{on } \Gamma_{outlet} \tag{14}$$

In eq. 13, e_i is the vector pointing in the direction of the lift force. In several test calculations it has been found that the complex outflow condition (eq. 14) could be replaced by a simple Neumann condition, which gives much better numerical convergence. If the pressure reference point is put near the outlet and the adjoint pressure is fixed to zero at this location, no significant change in the flow field could be observed. In order to reduce the numerical expense, only the effective viscosity of the RANS-solution is used in equation 11 and the adjoint transport equations of k and ω are dropped.

In each optimization cycle, the RANS-equations have to be solved in a forward run and the convective fluxes and the velocity gradients have to be stored. Due to the mathematical similarity of the RANS- and adjoint equations the subsequent backward computation of the adjoint system is performed with a method in many ways analogous to that of the forward run.

The derivative of the objective function with respect to the control f is

$$\nabla_f J = -\mu_{eff}\left(\frac{\partial w_i}{\partial x_j} + \frac{\partial w_j}{\partial x_i}\right)n_j + qn_i - \varrho f_j n_j w_i - \varrho f_j w_j n_i \tag{15}$$

American Institute of Aeronautics and Astronautics

As the suction angle β is the parameter to be optimized for the steady case, it follows for the derivative with respect to β:

$$\frac{\partial J}{\partial \beta} = \int_{\Gamma_{slot}} \nabla_f J \nabla_\beta f \, ds \approx \sum_{\Gamma_{slot}} \nabla_f J \nabla_\beta f \, \Delta s \tag{16}$$

IV.   Results

A.   Steady Case

Prior to the optimization, several computations with varying suction angles have been performed to characterize the flow field and to obtain the lift coefficient c_l as a function of β. This was done for $\alpha = 9°$ and $\alpha = 14°$, in the following referred to as 9°-case and 14°-case. In fig. 4 the velocity magnitude and streamlines of the base flow and different suction angles are shown for the 14°-case. In the base flow a large recirculation zone exists, which covers approximately half of the suction side. When steady suction is applied at the perturbation slot the separation moves downstream and the size of the recirculation zone decreases, see fig. 4(b). By increasing the suction angle the size of the separation bubble can be further reduced although the change is relatively small between $\beta = 60°$ and $\beta = 90°$. With the chosen perturbation amplitude it is not possible to eliminate the separation completely. A convenient possibility to highlight the isolated effect of the perturbation is to plot the difference of flow quantities of the base flow and the perturbed flow, calculated according to

$$\phi_{diff} = \phi_{base} - \phi_{pert} \tag{17}$$

In fig. 5 this is done for the normalized velocity magnitude $u_{abs,diff}/u_\infty$. Red color corresponds to positive and blue color to negative values. It is obvious that the flow is strongly accelerated in the vicinity of the separation as well as in the wake of the airfoil. At the maximum suction angle the velocity increase is of the same order of magnitude as the free stream velocity. There is also an significant increase of the velocity in the region upstream of the suction slot of up to 25% of the free stream velocity. On the pressure side the flow is slightly decelerated.

The influence of the steady suction on the pressure field is illustrated by the difference in the pressure coefficient in fig. 6. In the region around and upstream of the suction slot the pressure is strongly decreased by up to 90% of the baseline c_p due to the acceleration of the flow. On the pressure side there is a slight increase of the pressure caused by the deceleration of the fluid. As the main fraction of the lift stems from the pressure force it can be concluded that there is a significant influence of the suction angle on the lift coefficient.

As can be seen from the lift coefficient in fig. 7(a), a lift gain of 27% ($\alpha = 9°$) to 30% ($\alpha = 14°$) can be achieved by steady suction at the optimal angle. Note, that $\beta = 0°$ and $\beta = 180°$ in fig. 7(a) correspond to the base flow. For the 9°-case, the lift curve is very similar to a parabola, while it is more shallow in the vicinity of the peak for the 14°-case. This can also be seen from the gradient of the lift coefficient in fig. 9. However, both curves are symmetric with respect to the optimum suction angle. Therefore, only angles from $\beta = 0°$ to $\beta = 90°$ will be discussed in the following.

The location of the optimum suction angle is related to the mass flux through the perturbation slot because the flux is proportional to the inner product of the velocity vector and the unit normal vector of the slot surface. Thus, the variation of β results in a variation of the mass flux, see fig. 7(b). The most significant improvement in lift can be achieved for suction angles between $\beta = 0° - 60°$, which correlates quite well with the mass flux. The optimal suction angle is $\beta = 90°$, i.e. normal to the slot surface. Although this parameter choice might lack practical relevance, it is convenient for testing the optimization methods, because it gives a prominent maximum of lift at the optimal suction angle.

The lift gain only partly correlates with the size of the recirculation zone. This is indicated by the separation point shown in fig. 7(c) as well as by the contour plots in figs. 4 and 5. For both AoA the separation position stagnates for relatively low suction angles whereas the lift further increases. This can be explained by the upstream acceleration of the flow, which is caused by the suction.

It should be noted that the identification of the separation point was ambiguous for the high suction angles of the 9°-case. This is due to the sharp trailing edge of the airfoil which causes numerical problems in the form of pressure and velocity oscillations. Although these are limited to a small region around the trailing edge they caused problems for the 9°-case, because the separation point is located in this area for $\beta > 40°$.

American Institute of Aeronautics and Astronautics

The c_p-distribution on the surface of the airfoil (fig. 7(d)) again shows that the main effect of the steady suction is the pressure decrease upstream of the slot due to the acceleration of the flow. Downstream of the perturbation the reduction of the recirculation zone can be identified by the smaller plateau in the c_p-progression. However, the pressure coefficient only shows a significant dependency on the suction angle in the region upstream of the perturbation. It should be pointed out that there are strong pressure oscillations near the slot. These are caused by the sudden change of the velocity from zero at the wall to the slot velocity. The use of a velocity profile instead of constant values for u and v at the slot might help to reduce the oscillations. Furthermore, the grid resolution near the slot is not sufficient and it is assumed that the wiggles can be further decreased by refining the grid.

Fig. 8 gives an impression of the adjoint velocity magnitude of the base flow and different suction angles. In the context of lift improvement, high adjoint velocities indicate a strong sensitivity with respect to an additional volume force. In the base flow the high adjoint velocity is restricted to a narrow region close to the wall on the suction side of the airfoil and to the stagnation point streamline. This indicates that an acceleration of the flow in this area could significantly improve the lift. Further away from the surface the sensitivity rapidly tends to nearly zero. The application of the steady suction results in a massive decrease of the adjoint velocity upstream of the slot. Especially near the wall the velocity drops close to zero. With increasing suction angle the area of low adjoint velocity near the wall broadens slightly while it remains nearly unchanged downstream of the perturbation position.

A comparison of the gradient of the lift coefficient obtained from the two different optimization strategies is shown in fig. 9. The gradient descent method uses a finite difference to calculate the gradient whereas eq. 16 is used for the adjoint method. Although the order of magnitude of the gradients does not match exactly, the qualitative agreement is very good. However, the zero-intersection differs slightly. The gradient descent method hits exactly the correct angle of $\beta = 90°$ while the gradient of the adjoint method becomes zero at $\beta \approx 92°$. This might be caused by the oscillations in the vicinity of the slot (see fig. 7(d)) and will have to be investigated in future studies. Nevertheless, the deviation is only approx. 2% and one has to keep in mind that the gradient descent method will not be significantly more accurate. The increment $\Delta\beta$ should not be much lower than about one, as this would give much too slow convergence due to the limitation of the change in β, see eq. 7. Furthermore, excessively small increments could cause numerical problems for the evaluation of the finite difference in eq. 6, if the objective function is not perfectly smooth.

Fig. 10 shows results of the optimization with the adjoint method for both AoA. In these computations constant weighting factors of $\gamma = 100$ for $\alpha = 9°$ and $\gamma = 50$ for $\alpha = 14°$ were chosen, respectively. The optimization results are represented by the solid lines and the lift obtained by manual variation of β is included as dashed line for comparison. The suction angle is normalized such that $\beta^* = 0$ represents the start (or baseline) value and $\beta^* = 1$ is the target value. The same was done for the lift coefficient. The plots clearly show the monotonic improvement of c_l and β during the optimization, although the target angle is approached rather slowly. It is nearly reached after 20 to 30 cycles but is never hit exactly as the gradient crosses zero at $\beta \approx 92°$ (see above). However, the convergence of the lift is much better. After only three to four optimization cycles the normalized lift already reaches around 90% of the target value. With about six to eight additional iterations the desired lift is nearly reached and the remaining iterations are used for only marginal improvement. This is caused by the low slope of the lift curve between $60°$ and $120°$ where the c_l^* changes only around 10%. If a stop criterion of $\epsilon = 0.01$ is selected the optimization is converged before the optimum suction angle is reached. This is highlighted by the vertical lines in fig. 10.

Fig. 11 presents results of the optimization of the $9°$-case using the gradient descent method. Several runs with different start value, increment and weighting factor have been computed, in the following referred to as run1 ($\beta_{start} = 30$, $\Delta\beta = 5$, $\gamma = 20$), run2 ($\beta_{start} = 60$, $\Delta\beta = 1$, $\gamma = 200$) and run3 ($\beta_{start} = 60$, $\Delta\beta = 5$, $\gamma = 20$). As for the adjoint strategy the vertical lines indicate convergence for a stop criterion of $\epsilon = 0.01$. Run2 and run3 have been continued beyond this level in order to study the convergence of the suction angle. It is interesting to see that only run2 was successful in optimizing towards the correct suction angle. Run1 converged so slowly that the stop criterion of $\epsilon = 0.01$ was reached before the optimum lift coefficient. Run3 demonstrates problems which arise from a non-monotonic progression of the objective function. The sharp trailing edge of the airfoil causes numerical oscillations of the velocities and pressure near the trailing edge (see above). In the $9°$-case the separation point is located exactly in this region for $40° \leq \beta \leq 140°$. As the variation of β between $60°$ and $120°$ causes only small changes in the flow, these oscillations are also to be found in the lift coefficient. Depending on the choice of the optimization parameters the method occasionally optimizes towards one of these wiggles, see fig. 13. For the $14°$-case, depicted in fig. 12, such a behavior

could not be observed. Two of three investigated parameter combinations converged to the desired value. Only the third reached the stop criterion of $\epsilon = 0.01$ before the optimum suction angle, similar to run1 of the 9°-case, but might have converged for a lower ϵ.

The computation times for one cycle of the both methods is of the same order of magnitude, i.e. the convergence of the adjoint calculations is comparable to that of the RANS-calculations. Approximately 0.4 CPUh were needed to obtain a single solution of the flow field. For an optimization with 50 cycles on 4 CPUs, a total time of 40 CPUh or 10h wall clock time was used. It should be pointed out, that there is still room for improvement concerning the computation time, if higher values for γ are chosen.

B. Unsteady Case

The unsteady test case has been previously investigated numerically as well as experimentally by Tinapp, Schatz and Petz.[4, 5, 8] In these studies the underlying flow physics has been analyzed in detail. Although the setup of the present high-lift configuration differs slightly from that used by Schatz[4] in terms of turbulent inlet conditions, treatment of transition and turbulence modeling, the basic features are very similar. Thus, only a short summary of the main features will be given here and the interested reader is referred to these publication for a more detailed analysis of the flow physics.

The snapshots of the spanwise vorticity presented in fig. 14 give a good impression of the flow characteristics. On the main profile the flow remains quasi steady and attached. Due to the high flap deflection the flow separates near the flap's leading edge. Because of the complex interaction of the shear layers of the main profile and the flap the flow rapidly becomes unstable and big vortices develop. In contrast to the steady suction, which can be interpreted as acceleration or suction of the boundary layer, the periodic perturbation is a dynamic concept. In the present case it aims to exploit the instability inherent to the flow, whereby the predominant structures are to be amplified in order to increase the mixing and reduce the recirculation zone. In fig. 14(b) the effect of optimal periodic excitation is illustrated. The intensity of the vortices is stronger compared to the base flow and the recirculation zone has significantly decreased. The flow angle behind the trailing edge is notably higher which is an indicator for an increase of the lift force.

As for the steady test case, a set of computations with varying perturbation parameters have been conducted prior to the optimization. Fig. 15(a) shows the dependency of the lift coefficient on the non-dimensional perturbation frequency, which has been computed with a constant amplitude of $C_\mu = 50 \cdot 10^{-5}$. Obviously, it is not possible to find the global maximum with one of the methods used here, because the lift has four different maxima and the curve is not very smooth. However, the characteristic of c_l over C_μ presented in fig. 15(b) is much better suited for a gradient-based optimization. In these simulations the perturbation frequency was $St = 0.55$. The c_l-curve has a steep slope at low amplitudes and a prominent peak at $C_\mu = 50 \cdot 10^{-5}$. At the end of the tested range there is a sudden decrease of the lift coefficient.

A variety of optimization runs with different combinations of the increment ΔC_μ and weighting factor γ have been conducted for the generic high-lift configuration. The results of these computations are summarized in fig. 16. The runs with the lowest weighting factor $\gamma = 10$ converged very slowly and reached the stop criterion before the optimum C_μ. It is assumed that these optimizations would have converged to the correct value if the stop criterion had been set to a lower ϵ. For the remaining calculations only about three cycles were needed to approach the target value of c_l and C_μ, respectively.

The expense for one computation of the flow field was approximately 48 CPUh. As one optimization cycle consists of two calculations it follows that an optimization can be performed in about 300 CPUh, if the choice of the increment ΔC_μ and weighting factor γ is good. The slowly converging runs stopped after 1344 CPUh without reaching the optimum. This again emphasizes the importance of the choice of γ.

V. Conclusion

The concept of active flow control has been applied to two aerodynamic flow configurations in order to delay the separation of the flow and to increase the lift.

First the steady flow around a NACA4412 at $Re = 10^6$ was investigated, where the separation was successfully controlled by steady suction upstream of the separation. In a series of simulations the suction angle was varied from $\beta = 20°$ to $\beta = 160°$ and it was found that suction perpendicular to the slot surface is optimal. A gradient descent method and a strategy based on adjoint equations have been applied to the steady test case and have been successful in optimizing the suction angle.

The second test case was the unsteady flow around a generic high-lift configuration, where a dynamic concept using periodic blowing and suction could effectively reduce the massive separation at the flap. In extensive computations the amplitude and frequency of the harmonic perturbation have been varied and the optimum was identified. The gradient descent method was then applied to the unsteady configuration and was successful in finding the optimal perturbation amplitude.

For both test cases the convergence and computation times for the optimization runs varied widely, mainly depending on the weighting factor. However, only few iterations are needed if the optimization parameters are well chosen and the accuracy requirements for the optimal value are moderate.

Acknowledgments

References

[1]Becker, R., King, R., Petz, R. and Nitsche, W., *Adaptive Closed-Loop Separation Control on a High-Lift Configuration using Extremum Seeking*, AIAA paper 2006-3493, 2006.

[2]Bewley, T.R., Moin, P. and Temam, R., *DNS-based predictive control of turbulence: an optimal benchmark for feedback algorithms*, JFM, Vol. 460, 2002.

[3]Hinze, M. and Kunisch, K., *Second-order methods for optimal control of time-dependent fluid flow*, SICON, Vol. 40, 2001.

[4]Schatz, M. and Thiele, F., *Numerical Study of High-Lift Flow with Separation Control by Periodic Excitation*, AIAA paper 2001-0296, 2001.

[5]Schatz, M., Thiele, F., Petz, R. and Nitsche, W., *Separation Control by Periodic Excitation and its Application to a High-Lift Configuration*, AIAA paper 2004-2507, 2004.

[6]Schatz, M., Günther, B. and Thiele, F., *Computational investigation of separation control for high-lift airfoil flows*, Active Flow Control, Springer, 2006.

[7]Collis, S.S., Ghayour, K., Heinkenschloss, M., Ulbrich, M. and Ulbrich, S., *Optimal control of unsteady compressible viscous flows*, Int. J. Numer. Meth. Fluids, Vol. 40, 2002.

[8]Tinapp, F.H. and Nitsche, W., *On active control of high-lift flow*, In W. Rodi and D. Laurence, editors, Proc. 4th Int. Symposium on Engineering Turbulence Modelling and Measurements, Corsica, Elsevier Science, 1999.

[9]Wachsmuth, D., *Analysis of the SQP-method for optimal control problems governed by the instationary Navier-Stokes equations based on L^p-theory*, Preprint 13-2004, Institut für Mathematik, TU Berlin, submitted, 2004.

[10]Wachsmuth, D., *Optimal control of the unsteady Navier-Stokes equations*, PhD-Thesis, TU Berlin, Institute of Mathematics, 2006.

[11]Wassen, E. and Thiele, F., *Active control of a model vehicle wake*, to be published in: Journal of Turbulence, 2006.

[12]Wilcox, D.C., *Reassessment of the Scale-Determining Equation for Advanced Turbulence Models*, AIAA Journal, 26(11), p. 1299-1310, 1988.

[13]Xue, L., *Entwicklung eines effizienten parallelen Lösungsalgorithmus zur dreidimensionalen Simulation komplexer turbulenter Strömungen*, PhD thesis, Institute of Fluid Mechanics and Engineering Acoustics, Technical University of Berlin, 1998.
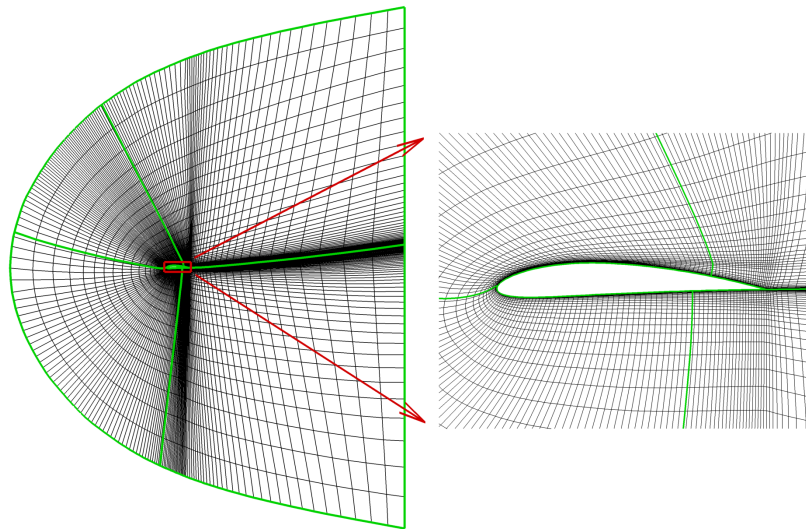
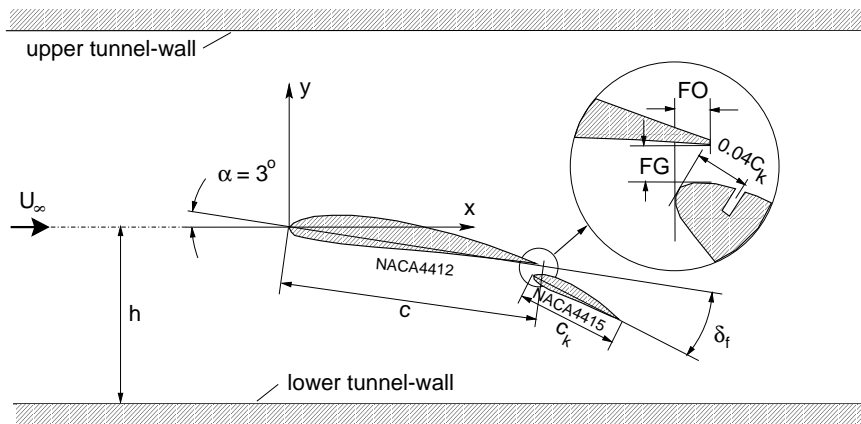**Figure 1. Computational mesh for the NACA4412, every 2nd grid point**

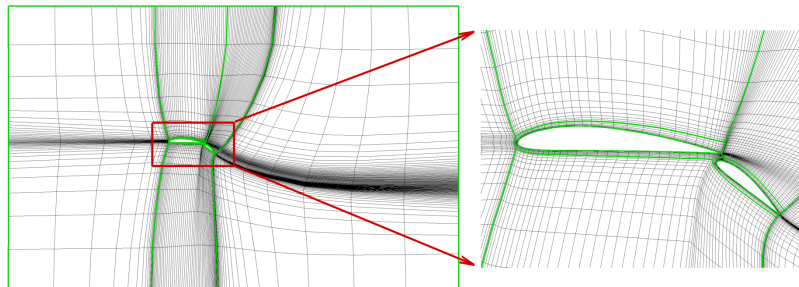**Figure 2. Sketch of the generic high-lift configuration**

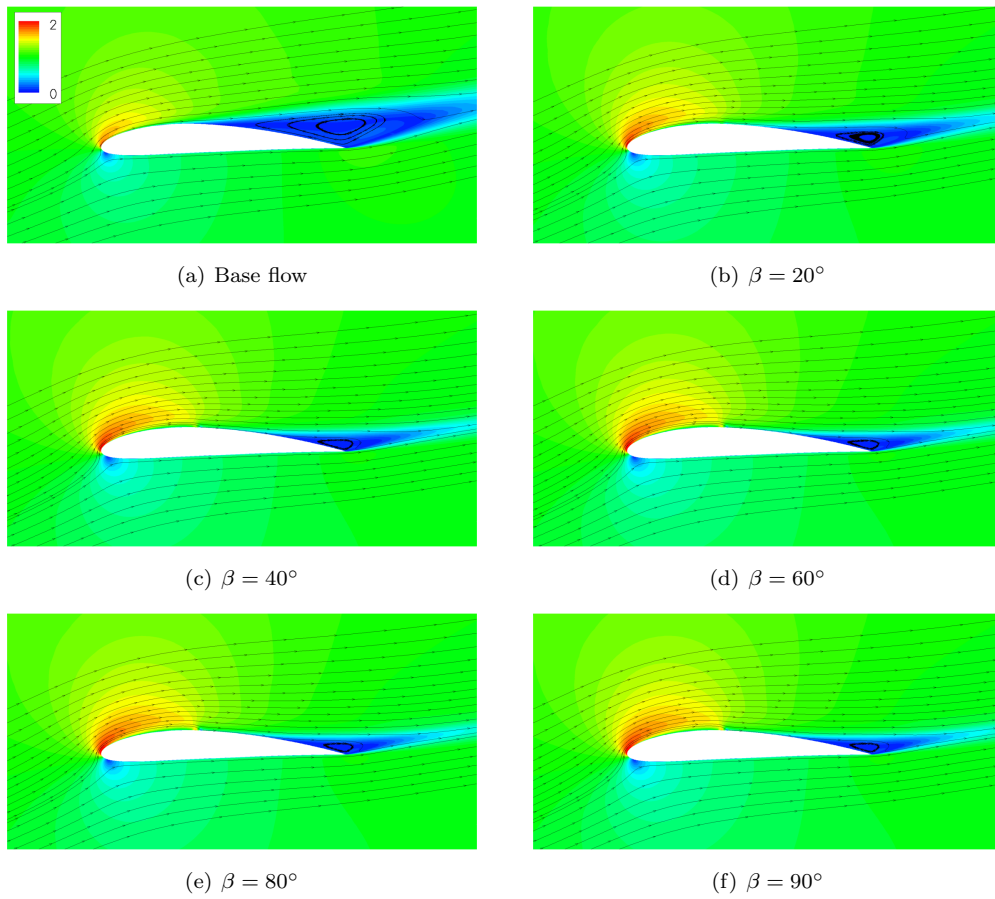**Figure 3. Computational mesh for the generic high-lift configuration, every 2nd grid point**

American Institute of Aeronautics and Astronautics

(a) Base flow

(b) $\beta = 20°$

(c) $\beta = 40°$

(d) $\beta = 60°$

(e) $\beta = 80°$

(f) $\beta = 90°$

Figure 4. Velocity magnitude and streamlines

(a) $\beta = 20°$

(b) $\beta = 40°$

(c) $\beta = 60°$

(d) $\beta = 90°$
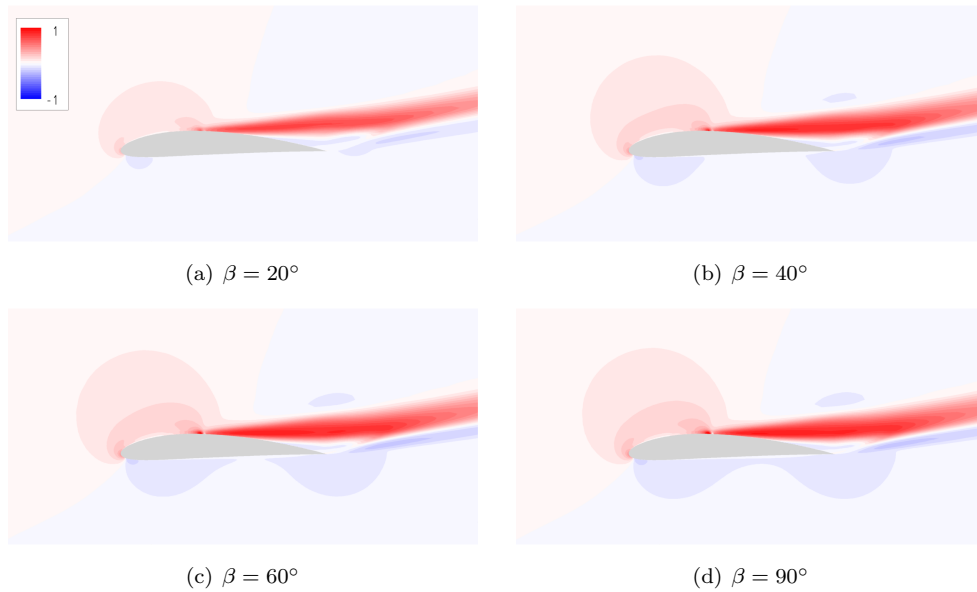
Figure 5. Difference in the velocity magnitude

American Institute of Aeronautics and Astronautics

(a) $\beta = 20°$

(b) $\beta = 40°$

(c) $\beta = 60°$

(d) $\beta = 90°$
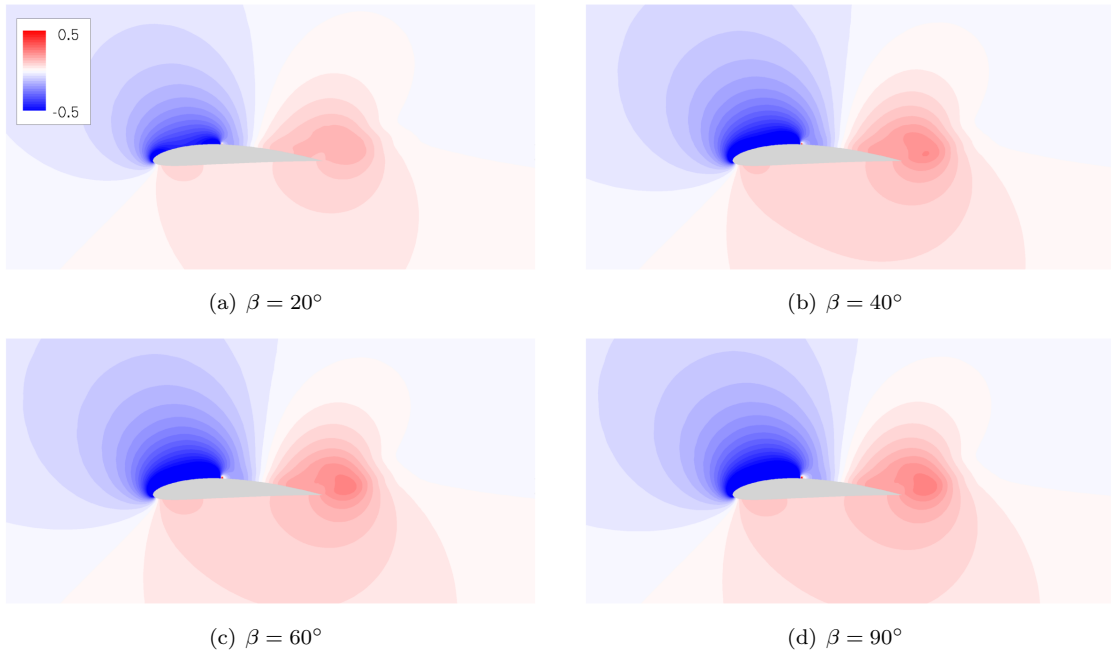
Figure 6. Difference in the pressure coefficient

(a) Normalized lift coefficient

(b) Normalized flux

(c) Separation point

(d) Pressure coefficient

Figure 7. Surface data

(a) Base flow

(b) $\beta = 20°$

(c) $\beta = 40°$

(d) $\beta = 60°$

(e) $\beta = 80°$

(f) $\beta = 90°$
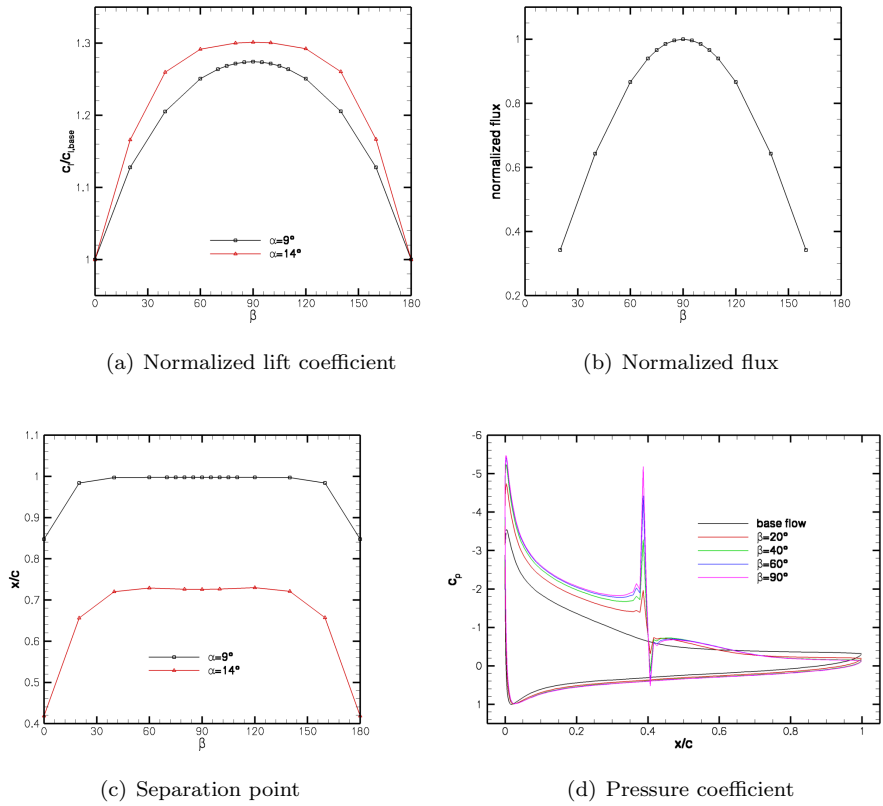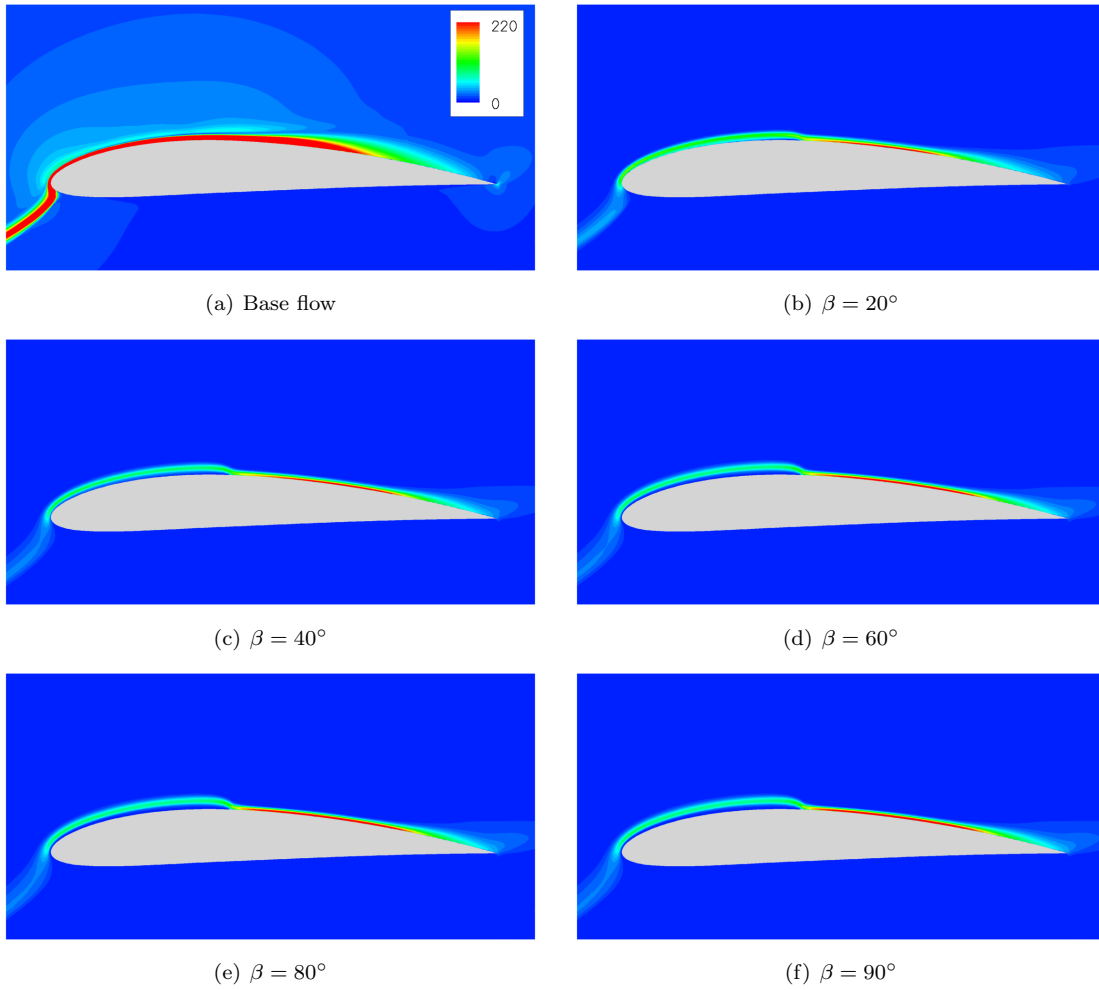
Figure 8. Adjoint velocity magnitude
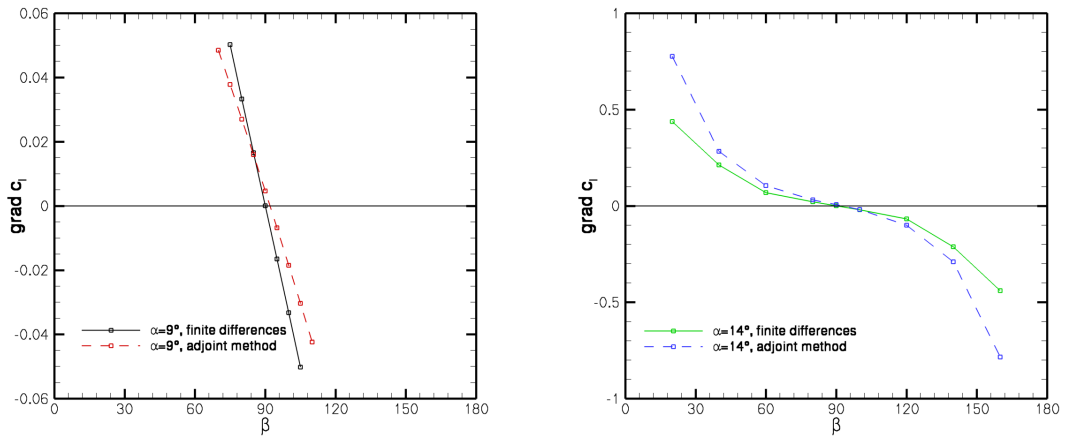
Figure 9. Gradient of the lift coefficient
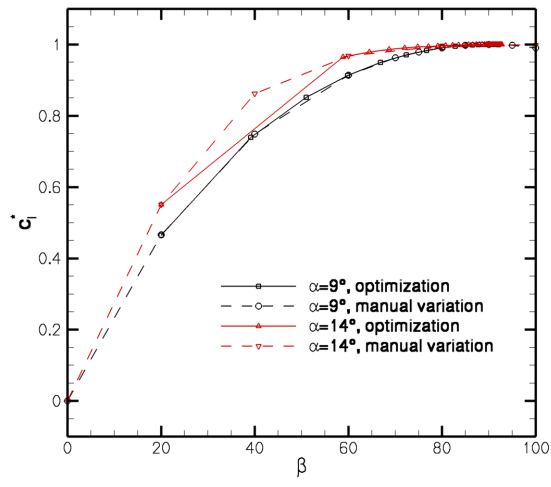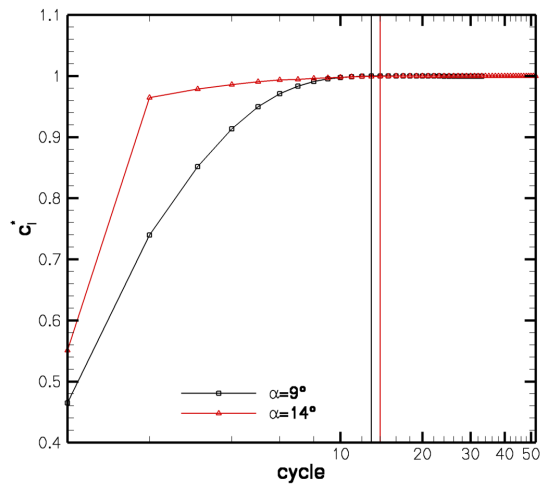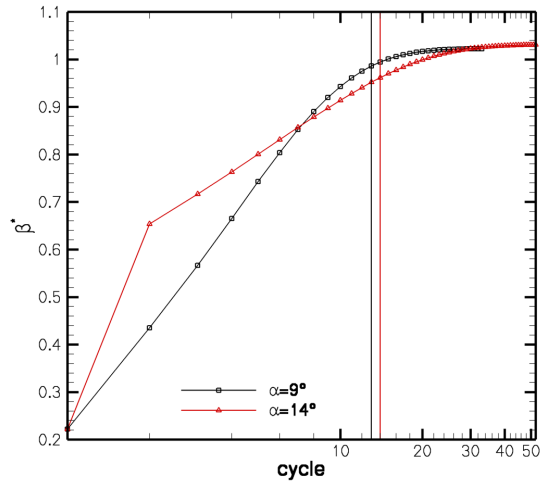
Figure 10. Optimization with the adjoint method
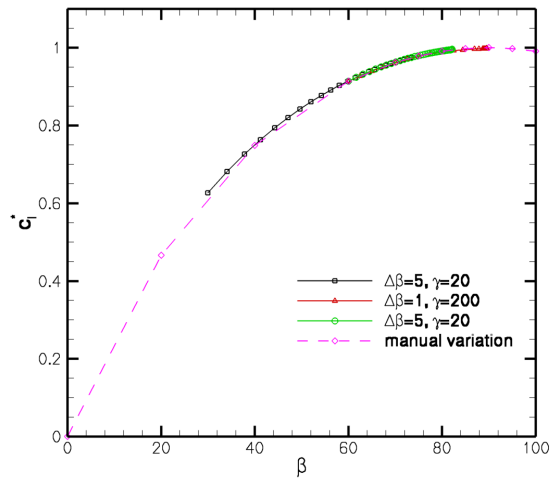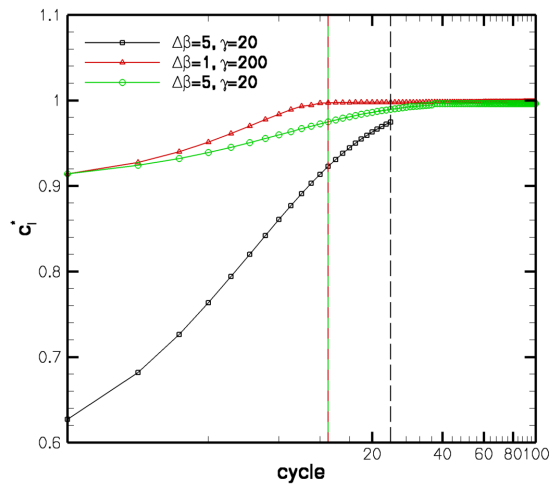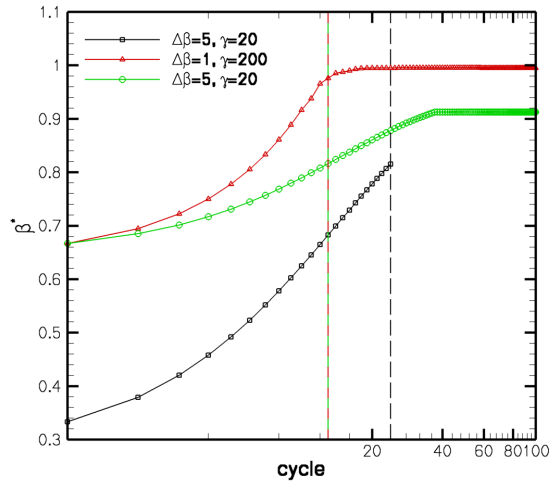
Figure 11. Optimization with the gradient descent method, $9°$-case
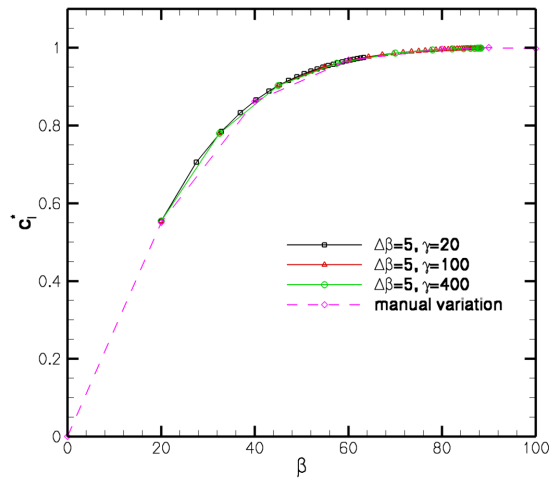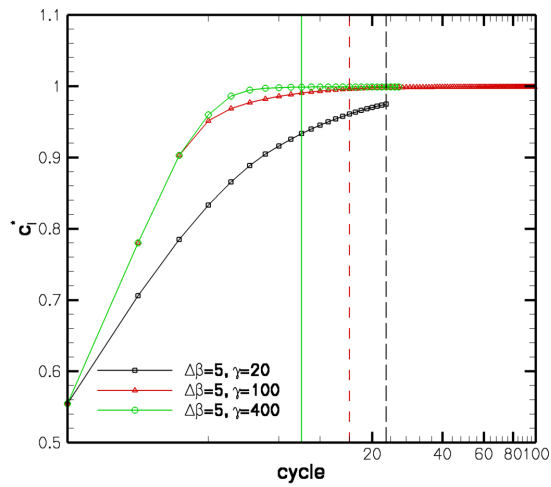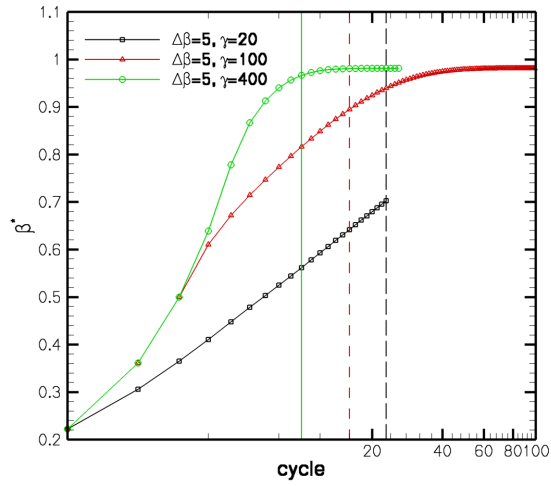
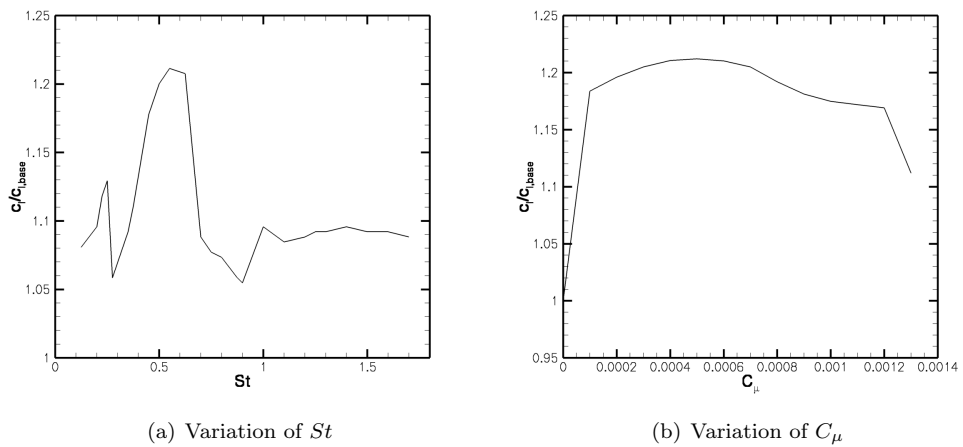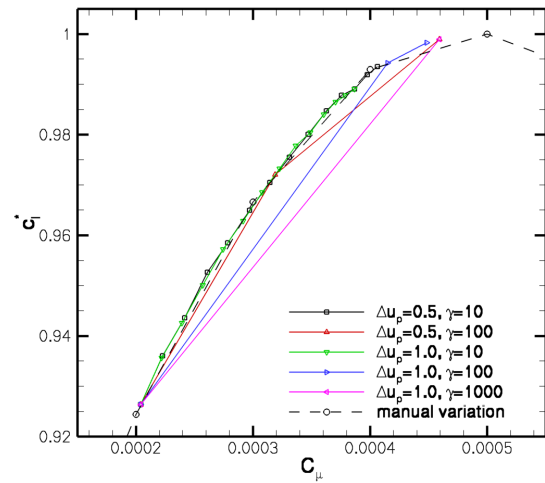**Figure 12. Optimization with the gradient descent method, $14°$-case**
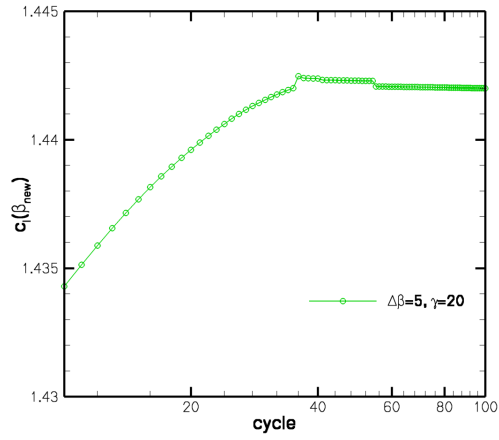
Figure 13. $c_l(\beta_{new})$ **over cycles, $9°$-case**
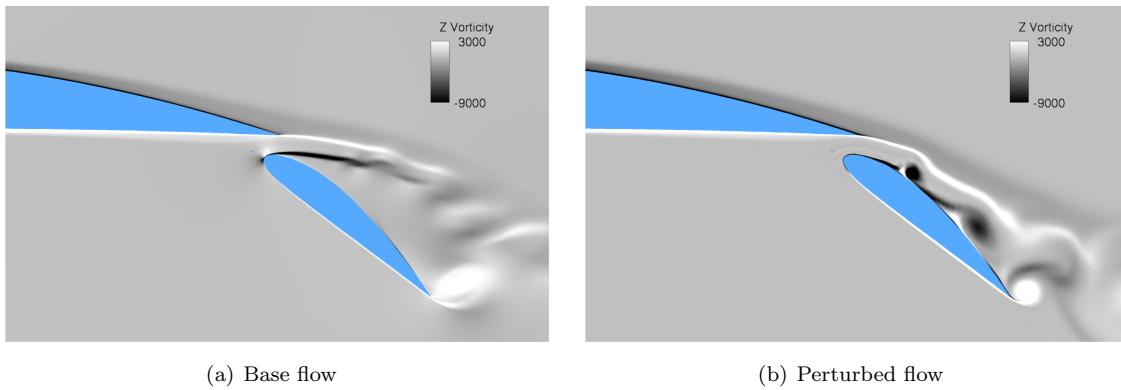
(a) Base flow

(b) Perturbed flow

Figure 14. Snapshots of the spanwise vorticity

(a) Variation of St

(b) Variation of C_μ

Figure 15. Dependency of the lift coefficient on the perturbation parameters
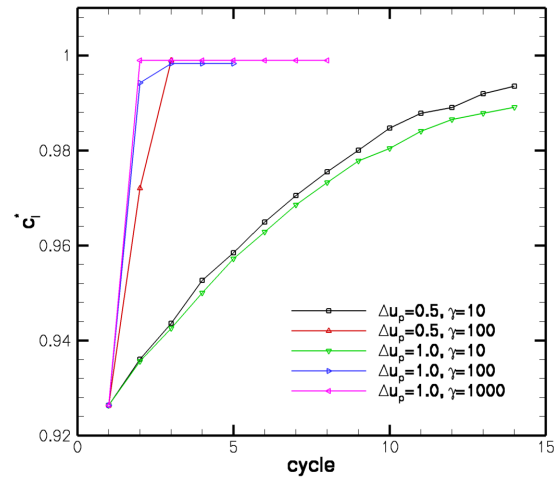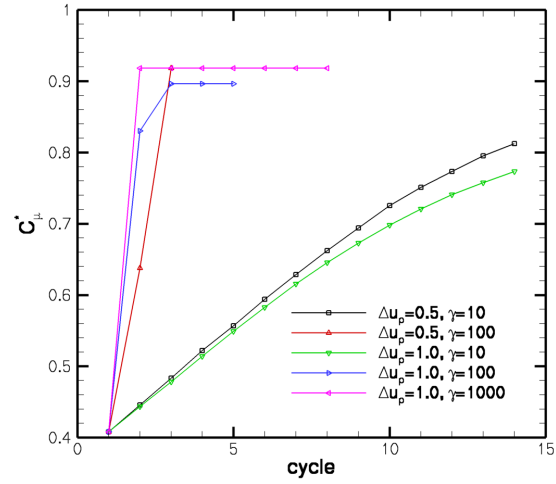
American Institute of Aeronautics and Astronautics

Figure 16. Optimization with the gradient descent method